New Constitutive Model for Interface Elements in Finite-Element Modeling of Masonry

Nitin Kumar, S.M.ASCE[1]; and Michele Barbato, M.ASCE[2]

Abstract: A new interface element constitutive model is proposed in this study for analyzing masonry using the simplified micromodeling (SMM) approach, in which mortar and two unit–mortar interfaces are lumped into a zero-thickness joint (modeled using an interface element) between expanded masonry units. The new model is capable of simulating tension cracking, shear slipping, and compression failure, and is defined by a convex composite failure surface consisting of a tension-shear and a compression cap failure criterion. It removes the singularity in the tension-shear region but not in the compression-shear region. In addition, the proposed model is based on the hypothesis of strain hardening. The robustness and computational cost of the proposed model were compared with different constitutive models (which are based on three, two, and one failure criteria) that have been widely used in the literature to describe masonry behavior through a series of one-element tests and through the comparison of finite-element (FE) response simulation of an unreinforced masonry shear wall. The FE response results indicate that the proposed constitutive model is more efficient than and at least as accurate as the other constitutive models for analyzing masonry using the SMM approach. **DOI: [10.1061/(ASCE)EM.1943-7889.0001592](#).** © *2019 American Society of Civil Engineers.*

Author keywords: Finite-element method; Simplified micromodeling; Interface element; Constitutive model; Masonry walls.

Introduction

Finite-element (FE) modeling of masonry structures is a very complex problem in computational mechanics which continues to attract the interest of the research community after several decades of investigations. Several FE approaches have been proposed, with different levels of accuracy, computational cost, and information details (Lourenço 1996; Pelà 2009). The highest level of accuracy and detail of the mechanical behavior of masonry can be achieved using the FE micromodeling approach, in which different masonry components, i.e., masonry units (bricks/blocks) and mortar, are distinctly represented through continuum elements, and the unit–mortar interface is represented by interface elements (Lourenço 1996). Thus, micromodeling explicitly addresses the intrinsic discontinuity and heterogeneity of masonry elements. However, it is also computationally very intensive, and thus is rarely employed for analyzing masonry. The computational cost can be reduced by lumping mortar and two unit–mortar interfaces into a zero-thickness joint (generally modeled using an interface element) between expanded masonry units (Page 1978; Lourenço 1996). This modeling approach is referred to as simplified micromodeling (SMM) and has been widely employed to investigate the local behavior of masonry (Page 1978; Lourenço 1996; Giambanco et al. 2001; Spada et al. 2009; Dolatshahi and Aref 2011; Macorini and Izzuddin 2011; Aref and Dolatshahi 2013; Kumar et al. 2014b).

The capability of the SMM approach to simulate the mechanical response of masonry properly relies upon the accuracy and robustness of the employed interface element, which relates the traction vector to the relative displacement vector. In fact, in most SMM approaches, the nonlinearity of the system is often concentrated in the interface element, and masonry units are assumed to be elastic in nature (Page 1978; Lotfi and Shing 1994; Lourenço 1996; Chaimoon and Attard 2007; Dolatshahi and Aref 2011; Macorini and Izzuddin 2011). Hence, interface elements should be able to describe all major failure mechanisms of masonry under multiaxial stress conditions (Page 1983; Dhanasekar et al. 1985; Andreaus 1996; Lourenço 1996; Cuellar-Azcarate 2016), which include (1) cracking of masonry units in direct tension, (2) cracking of mortar joints, (3) bed or head joint failure due to sliding under normal stress, (4) diagonal tension cracking of masonry units, and (5) masonry crushing.

Zero-thickness interface elements formulated in terms of traction-separation relationships were originally introduced by Goodman et al. (1968) to model discontinuity in rock mechanics. Page (1978) introduced the use of interface elements between elastic continuum elements (representing expanded masonry units) in failure analysis of masonry. The nonlinear behavior of masonry was simulated through the interface behavior, which was modeled through a constitutive model that included a brittle failure in tension and hardening in shear/compression. However, compression (crushing) failure was not included in the interface elements (e.g., Page 1978; Lotfi and Shing 1994; Anand and Yalamanchili 1996; Giambanco and Di Gati 1997) until an appropriate constitutive model for analysis of masonry shear walls was developed by Lourenco and Rots (1997) to simulate/predict the ultimate strength and postpeak behavior of masonry. The Lourenco and Rots model is a multisurface composite interface model (CIM) that consists of three different failure criteria (failure surfaces), i.e., a Rankine failure criterion (tension cut-off criterion) for Mode-I failure (opening in tension), a Mohr–Coulomb failure criterion for Mode-II failure (in plane shearing or sliding), and a compression cap failure criterion for compression failure. The Rankine and the Mohr–Coulomb failure surfaces are coupled through internal softening

[1]Ph.D. Scholar, Dept. of Civil and Environmental Engineering, Univ. of California, Davis, One Shields Ave., Ghausi Hall, Davis, CA 95616. ORCID: https://orcid.org/0000-0002-4045-300X. Email: ntnkumar@ucdavis.edu

[2]Professor, Dept. of Civil and Environmental Engineering, Univ. of California, Davis, One Shields Ave., 3149 Ghausi Hall, Davis, CA 95616 (corresponding author). Email: mbarbato@ucdavis.edu

parameters, whereas the Mohr–Coulomb and the compression cap failure surfaces are uncoupled. This multisurface CIM has been used by many researchers to investigate the behavior of masonry structures (Oliveira and Lourenço 2004; Furukawa et al. 2010; Dolatshahi and Aref 2011; Tarque 2011; Miccoli et al. 2015).

Numerous interface element constitutive models (based on numbers of failure surfaces, different failure criteria, and softening/hardening hypotheses) have been proposed to investigate the behavior of masonry by using the SMM approach. The simplest approach in defining an interface element constitutive model is to adopt one failure surface to describe each of the three major failure mechanisms, i.e., tension, shear, and compression, (Lourenço 1996; Oliveira and Lourenço 2004; Chaimoon and Attard 2007; Minga et al. 2018). However, the use of multiple failure surfaces leads to singularity problems at the intersections between two of these surfaces (Abbo and Sloan 1995). Therefore, several constitutive models were developed with failure surfaces representing two (Lourenço 1994; Macorini and Izzuddin 2011) or three (Citto 2008; Bakeer 2009; Kumar et al. 2014a) failure mechanisms at a time. The use of these more complex failure surfaces can introduce issues of robustness and may increase the computational cost of the constitutive model (Lourenço 1994).

This paper proposes a new interface element constitutive model that is capable of simulating tension cracking, shear slipping, and compression failure for masonry analysis using the SMM approach. The proposed constitutive model is developed within the framework of nonassociative elastoplastic materials with softening. Other approaches could be used to improve the efficiency and robustness of masonry modeling based on the SMM approach, e.g., the plasticity-damage approach (Gambarotta and Lagomarsino 1997a, b; Minga et al. 2018), the variational approach (Khisamitov and Meschke 2018), the damage approach (Greco et al. 2017; Khisamitov and Meschke 2018), and the elastoviscoplastic modeling approach (Shing and Manzouri 2004; Tang et al. 2007). However, the consideration of these alternative approaches is beyond the scope of this study. The robustness and computational cost of the proposed constitutive model are compared with those of different constitutive models that have been widely used in the literature to describe masonry behavior through a one-element test. In addition, the performance of the different constitutive models is investigated in terms of accuracy and computational cost by simulating an unreinforced masonry shear wall for which well-documented experimental results are available in the literature. Finally, conclusions are made based on the results obtained in the present study.

Research Significance

This paper introduces a novel mechanical constitutive model for interface elements used in the context of the SMM approach for masonry structures. The proposed constitutive model achieves robustness, computational efficiency, and accuracy in modeling masonry structures under multiaxial stress conditions by (1) overcoming the singularity problem that arises from the interaction between the Mohr–Coulomb failure criterion and the Rankine failure criterion, and (2) using the strain-hardening/softening hypothesis to improve the numerical robustness of the solution during the evolution of the yield surfaces. In addition, the proposed constitutive model is easily extendable to cyclic/hysteretic behavior. Therefore, the constitutive model developed here for interface elements can extend the use of the SMM approach to investigate the behavior of masonry components and structures.

This paper also investigates the advantages and disadvantages of different constitutive models for interface elements when using the
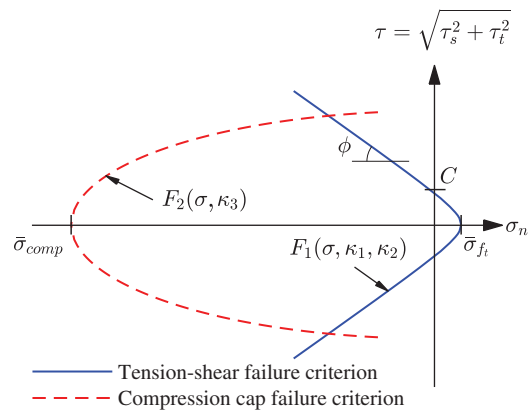

Fig. 1. Typical composite failure surface for the proposed CTSIM in stress space.

same integration scheme. This comparison provides useful information for further development of interface element constitutive models to simulate the mechanical behavior of masonry and other quasi-brittle materials.

Proposed Coupled Tension-Shear Interface Model

Interface elements permit discontinuities in the displacement field, and their behavior can be described in terms of a relation between the traction, $\boldsymbol{\sigma}$, and relative displacements, $\mathbf{u}$, across the interface. Thus, the generalized elastic behavior of the interface element constitutive model can be written in standard form as

$$\boldsymbol{\sigma} = \mathbf{k} \times \mathbf{u} \tag{1}$$

where, for a three-dimensional (3D) configuration, $\boldsymbol{\sigma} = \{\sigma, \tau_s, \tau_t\}^T$; $\mathbf{u} = \{u_n, u_s, u_t\}^T$; and $\mathbf{k} = \text{diag}[k_n, k_s, k_t]$, where $\text{diag}[\cdot]$ = diagonal matrix operator, n = normal components, and s and t = shear components in two orthogonal directions. The component of the elastic stiffness matrix, $\mathbf{k}$, for the constitutive model in the SMM approach can be obtained from the properties of the masonry components (i.e., masonry units and mortar), and can be written (Rots and Picavet 1997)

$$\frac{1}{k_n} = \left(\frac{h_m}{E_m} - \frac{h_m}{E_b} \right), \qquad \frac{1}{k_s} = \frac{1}{k_t} = \left(\frac{h_m}{G_m} - \frac{h_m}{G_b} \right) \tag{2}$$

where E_m and E_b = Young's modulus for mortar and masonry units, respectively; G_m and G_b = shear modulus for mortar and masonry units, respectively; and h_m = thickness of the mortar joints. Eq. (2) may significantly overestimate the elastic stiffness of the masonry joint's interface, particularly when the masonry units are weaker than the mortar or when the bond surface between mortar and units presents gaps (Rots and Picavet 1997; Chisari et al. 2018). Thus, several approaches have been proposed to obtain a better representation of the actual response of unreinforced masonry, e.g., by introducing a reduction factor in the calculation of the elastic stiffness based on Eq. (2) (Rots and Picavet 1997; Chaimoon and Attard 2007; da Porto et al. 2010), or by proposing more-refined model parameter calibration strategies (Chisari et al. 2015).

The inelastic behavior of the proposed constitutive model for interface elements, referred to as coupled tension-shear interface model (CTSIM) hereafter, is defined by a convex composite failure surface (Fig. 1), which consists of a tension-shear failure criterion $F_1(\boldsymbol{\sigma}, \kappa_1, \kappa_2)$ and a compression cap failure criterion $F_2(\boldsymbol{\sigma}, \kappa_3)$,

where κ_1, κ_2, and κ_3 are the scalar softening/hardening parameters. The selection of this composite failure surface, which removes the singularity in the tension-shear region but not in the compression-shear region, is based on the fact that the shear and tensile behaviors of masonry are coupled, whereas the compression and shear behaviors can be considered as uncoupled (Lourenço 1996). Thus, removing the singularity in the tension-shear region can reduce the computational cost of the interface element, whereas removing the singularity in the compression-shear region is not effective in reducing the computational cost of the interface element (Lourenço 1994). The specific form of $F_1(\boldsymbol{\sigma}, \kappa_1, \kappa_2)$ used in this study presents several novel characteristics compared with other existing models, and was used here for the first time in the context of interface elements for masonry modeled using the SMM approach.

Tension-Shear Failure Criterion

A single hyperbolic surface is used to represent pressure-dependent shear failure and tensile cracking. The use of this surface overcomes the singularity problem that occurs in multisurface failure criteria, i.e., in the combination of the Mohr–Coulomb and Rankine failure criterion (Abbo and Sloan 1995), and it enables the proposed interface element constitutive model to converge faster for larger load steps at the Gauss point level. The failure criterion originally proposed by Caballero et al. (2008) for the concrete fracture problem is adopted here for the first time to describe the tension-shear yield surface as

$$F_1(\boldsymbol{\sigma}, \kappa_1, \kappa_2) = -[C(\kappa_1, \kappa_2) - \sigma \cdot \tan\phi(\kappa_1, \kappa_2)] + \sqrt{\tau^2 + [C(\kappa_1, \kappa_2) - \bar{\sigma}_{f_t}(\kappa_1, \kappa_2) \cdot \tan\phi(\kappa_1, \kappa_2)]^2} \tag{3}$$

where $\tau^2 = \tau_s^2 + \tau_t^2$; ϕ = frictional angle; $\bar{\sigma}_{f_t}(\kappa_1, \kappa_2)$ = tensile yield stress; and $C(\kappa_1, \kappa_2)$ = cohesive yield stress. This hyperbolic failure criterion represents an improvement with respect to other criteria described by quadratic terms (Caballero 2005; Citto 2008; Macorini and Izzuddin 2011), which consist of two hyperbolic branches, only one of which has physical meaning. Therefore, this modified yield function relaxes the requirement for small load steps at the Gauss point level, which otherwise would be needed to guarantee that the computed stress is associated with the correct branch of the hyperbolic surface (Caballero et al. 2008). A strain-softening hypothesis is considered for this failure criterion, in which the normal and shear plastic relative displacements jointly control the softening of both tensile and cohesive yield stresses. The tensile and cohesive yield stresses are implicitly coupled, and softening in the tensile yield stress produces a proportional softening in the cohesive yield stress and vice versa. Thus, the rates of the scalar softening parameters are defined as follows by adapting the expressions originally derived by Lourenco (1996) to satisfy simultaneously the Mohr–Coulomb and Rankine failure criteria, respectively, at their singularity point:

$$\dot{\kappa}_1 = \langle \dot{u}_n^p \rangle + \frac{G_f^I}{G_f^{II}} \cdot \frac{C_0}{f_t} \cdot \sqrt{|\dot{u}_s^p|^2 + |\dot{u}_t^p|^2} \tag{4}$$

$$\dot{\kappa}_2 = \frac{G_f^{II}}{G_f^I} \cdot \frac{f_t}{C_0} \cdot \langle \dot{u}_n^p \rangle + \sqrt{|\dot{u}_s^p|^2 + |\dot{u}_t^p|^2} \tag{5}$$

where f_t = tensile strength; C_0 = initial cohesion; G_f^I = Mode-I fracture energy; G_f^{II} = Mode-II fracture energy; $\dot{u}_n^p$, $\dot{u}_s^p$, and $\dot{u}_t^p$ = plastic relative displacements in the n, s and t directions, respectively; $\langle \cdot \rangle$ are Macaulay brackets; and a superposed dot

indicates differentiation with respect to (pseudo)time. This form of the rates of the softening parameters allows their efficient computation when using a single smooth yield surface. In fact, the use of the Macaulay brackets ensures that the softening parameters are affected by tensile stresses in the shear-tension region, whereas they are not affected by compression stresses in the shear-compression region, consistent with the typical behavior of masonry joints (which are damaged by tension and shear stresses, but not by low compression stresses). The tensile yield stress $\bar{\sigma}_{f_t}(\kappa_1, \kappa_2)$ and cohesive yield stress $C(\kappa_1, \kappa_2)$ are respectively defined as

$$\bar{\sigma}_{f_t}(\kappa_1, \kappa_2) = f_t \cdot \exp\left[-\sqrt{\left(\frac{f_t}{G_f^I} \cdot \kappa_1\right)^2 + \left(\frac{C_0}{G_f^{II}} \cdot \kappa_2\right)^2}\right] \tag{6}$$

$$C(\kappa_1, \kappa_2) = C_0 \cdot \exp\left[-\sqrt{\left(\frac{f_t}{G_f^I} \cdot \kappa_1\right)^2 + \left(\frac{C_0}{G_f^{II}} \cdot \kappa_2\right)^2}\right] \tag{7}$$

The exponential terms are defined so to ensure that the tensile and cohesive yield stresses evolve in a proportional fashion (i.e., the shape of the yield function remains the same during the analysis) and include the effects of both softening parameters. The softening of the friction angle is assumed to be proportional to the softening of the cohesive yield stress, that is

$$\tan\phi(\kappa_1, \kappa_2) = \tan\phi_r + (\tan\phi_0 - \tan\phi_r) \cdot \frac{C(\kappa_1, \kappa_2)}{C_0} \tag{8}$$

where ϕ_0 = initial friction angle; and ϕ_r = residual friction angle. A nonassociative formulation is assumed for the tension-shear failure criterion because the friction angle, ϕ, and the dilatancy angle, ψ, are generally considerably different for masonry (Atkinson et al. 1989; Van der Pluijm et al. 2000). The plastic potential function $Q_1(\boldsymbol{\sigma}, \kappa_1, \kappa_2)$ is defined as (Caballero 2005)

$$Q_1(\boldsymbol{\sigma}, \kappa_1, \kappa_2) = -[C_Q(\kappa_1, \kappa_2) - \sigma \cdot \tan\psi(\kappa_1, \kappa_2)]^2 + \tau^2 + [C_Q(\kappa_1, \kappa_2) - \bar{\sigma}_{f_t}(\kappa_1, \kappa_2) \cdot \tan\psi(\kappa_1, \kappa_2)]^2 \tag{9}$$

where $C_Q(\kappa_1, \kappa_2)$ = apparent cohesive yield stress. The behavior of parameters C_Q and ψ is obtained by substituting C_Q and C_{Q0} for C and C_0, respectively, in Eq. (7), and substituting ψ, ψ_0 and ψ_r for ϕ, ϕ_0, and ϕ_r, respectively, in Eq. (8). The plastic potential function in Eq. (9) consists of quadratic terms, and, thus of two hyperbolic branches, similar to the failure yield criterion used, e.g., by Caballero (2005), Macorini and Izzuddin (2011), and Citto (2008), in which the same functional form was employed for both yield criterion and plastic potential function. However, because for the proposed CTSIM the yield criterion functional form is different from that of the plastic potential function, the existence of a non-physically meaningful branch does not introduce convergence issues. In fact, only because only the physically meaningful branch is actually used due to the constraints imposed by the consistency condition during the plastic-corrector step of the CTSIM's return mapping algorithm (Simo and Hughes 2006). The plastic potential function defined by Eq. (9) presents several computational advantages compared with other existing expressions, e.g., the derivatives of the plastic potential function with respect to stress are simpler than those for the plastic potential function proposed by Caballero et al. (2008).

Compression Cap Failure Criterion

The compression cap model used in the proposed constitutive model is described by an elliptical yield function originally
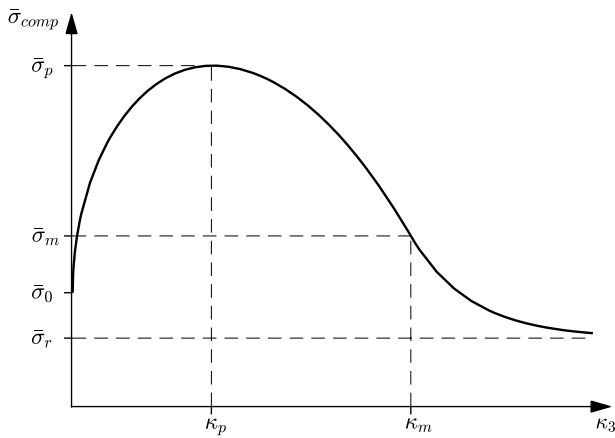
Fig. 2. Hardening/softening law for compression cap failure criterion.

introduced for orthotropic plasticity of soil materials (Schellekens 1992) as

$$F_2(\boldsymbol{\sigma}, \kappa_3) = C_{nn} \cdot \sigma^2 + C_{ss} \cdot \tau^2 + C_n \cdot \sigma - \bar{\sigma}_{comp}^2(\kappa_3) \qquad (10)$$

where C_{nn} and C_n = parameters that control the coordinates of the center of the compression cap failure surface; C_{ss} = parameter that controls the width of the cap failure surface in the shear stress axis; and $\bar{\sigma}_{comp}^2(\kappa_3)$ = compressive yield stress, which determines the width of the cap failure surface in the compressive stress axis. In this study, the center of the cap failure surface was assumed to coincide with the origin of the $\sigma - \tau$ plane with $C_{nn} = 1$ and $C_n = 0$, in order to avoid the activation of this surface in the tension-shear region, which is controlled by the tension-shear failure criterion described in the previous subsection. A strain-hardening/softening hypothesis is introduced for the compressive yield stress, which describes the rate of the corresponding scalar softening parameter as

$$\dot{\kappa}_3 = \sqrt{(\dot{u}_n^p)^2 + (\dot{u}_s^p)^2 + (\dot{u}_t^p)^2} \qquad (11)$$

and the compressive yield stress is defined as

$$\bar{\sigma}_{comp}(\kappa_3) = \begin{cases} \bar{\sigma}_0 + (\bar{\sigma}_p - \bar{\sigma}_0) \cdot \left(\dfrac{2\kappa_3}{\kappa_p} - \dfrac{\kappa_3^2}{\kappa_p^2} \right) & \text{if } \kappa_3 \le \kappa_p \\[2mm] \bar{\sigma}_p + (\bar{\sigma}_m - \bar{\sigma}_p) \cdot \left(\dfrac{\kappa_3 - \kappa_p}{\kappa_m - \kappa_p} \right)^2 & \text{if } \kappa_p < \kappa_3 \le \kappa_m \\[2mm] \bar{\sigma}_r + (\bar{\sigma}_m - \bar{\sigma}_r) \cdot \exp\left(m \cdot \dfrac{\kappa_3 - \kappa_m}{\bar{\sigma}_m - \bar{\sigma}_r} \right) & \text{if } \kappa_3 > \kappa_m \end{cases}$$

$$(12)$$

where $m = 2(\bar{\sigma}_m - \bar{\sigma}_p)/(\kappa_m - \kappa_p)$; $\bar{\sigma}_0$, $\bar{\sigma}_p$, $\bar{\sigma}_m$, and $\bar{\sigma}_r$ = initial (i.e., corresponding to the transition from linear to nonlinear behavior), peak, intermediate (i.e., corresponding to the inflection point in the softening branch), and residual compressive yield stresses, respectively; and κ_p and κ_m = total plastic strain at peak and intermediate compressive yield stress. Fig. 2 illustrates the evolution of the compressive yield stress, $\bar{\sigma}_{comp}$, as a function of the parameter κ_3. In Eq. (12), the first branch was taken from Lotfi and Shing (1991), whereas the second and third branches were taken from Lourenço (1996). An associative flow rule was assumed for the compression cap failure criterion, thus, $Q_2(\boldsymbol{\sigma}, \kappa_3) = F_2(\boldsymbol{\sigma}, \kappa_3)$.

The CTSIM was implemented in the commercial finite-element software package ABAQUS version 6.13 through a user-defined material subroutine (UMAT) written in FORTRAN (Metcalf et al. 2011) for an implicit integration scheme (Bathe 2006). The implicit backward Euler integration method (Simo and Hughes 2006) is used to integrate the different constitutive equations of the CTSIM, which leads to a system of nonlinear algebraic equations. These nonlinear equations are solved monolithically with the local/global Newton–Raphson technique as described by Ottosen and Ristinmaa (2005), Caballero et al. (2008), and Macorini and Izzuddin (2011), which leads to a combined local and global solution strategy. In addition, the CTSIM is combined with an adaptive substepping strategy to ensure convergence and accuracy of the final solution at both local and global levels (Pérez-Foguet et al. 2001; Caballero et al. 2008; Macorini and Izzuddin 2011).

Comparison of Constitutive Models Using One-Element Test

In this section, the robustness, computational cost, and accuracy of the CTSIM are compared with three interface element constitutive models that are available in the literature, namely the constitutive models proposed by Lourenco and Rots (1997), Macorini and Izzuddin (2011), and Citto (2008). Fig. 3 shows the typical failure surfaces corresponding to each of these constitutive models and compares them with the failure surface corresponding to the CTSIM. These failure surfaces are plotted using the following values of the material parameters: $C = 0.35$ MPa, $\bar{\sigma}_{f_t} = 0.25$ MPa, $\bar{\sigma}_{comp} = 3.50$ MPa, and $\tan \phi = 0.65$. The Lourenco and Rots model consists of three failure surfaces, as previously described in the "Introduction" section. The Macorini and Izzuddin model is defined by two hyperbolic failure surfaces (failure criteria), i.e., a tension-shear failure surface that represents Mode-I and Mode-II fracture, and a compression failure surface. Both failure surfaces shrink when the plastic work (which drives the softening of the material parameters) increases. The Citto model is composed of a single failure surface, which represents all three failure mechanisms of the interface element, i.e., Mode-I, Mode-II, and compression failure. The evolution of the hardening parameters is governed by a set of work-hardening/softening rules and the rate of plastic work (Citto 2008). Furthermore, the CTSIM and the Lourenco and Rots model use the hypothesis of strain hardening for the evolution of the hardening/softening parameters; whereas, the Macorini and Izzuddin and the Citto models use the hypothesis of work hardening. All these constitutive models were also implemented in the FE software ABAQUS by using a UMAT subroutine, similar to the implementation of the CTSIM, in order to provide a common platform for the comparison of these models with the CTSIM by removing the bias that could arise from the use of different integration schemes.

One-Element Test

In the following section, the performance of the different models is assessed through a one-element test. A single zero-thickness interface element was subjected to 13 different load paths defined by the angle $\theta = \arctan(u_\tau/u_n)$, where $u_\tau = \sqrt{u_s^2 + u_t^2}$ (Fig. 4), i.e., by considering a proportional increase of axial and shear relative displacements corresponding to $\theta = 0°$, $15°$, $30°$, $45°$, $60°$, $75°$, $90°$, $105°$, $120°$, $135°$, $150°$, $165°$, and $180°$. The relative displacement magnitude was incremented from $|\mathbf{u}| = 0$ mm to $|\mathbf{u}| = 0.2$ mm using a displacement control analysis. Four different load step sizes were considered by dividing the final relative displacements into 5, 10, 50, and 100 equal increments (designated N5, N10, N50, and N100 respectively). The material parameters corresponding to the
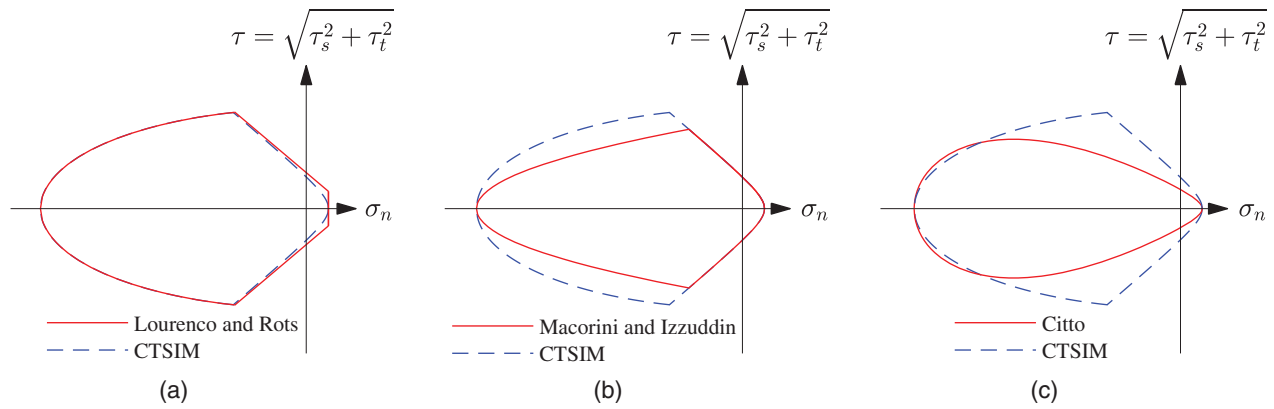
Fig. 3. Typical failure surface in stress space for (a) Lourenco and Rots model; (b) Macorini and Izzuddin model; and (c) Citto model.
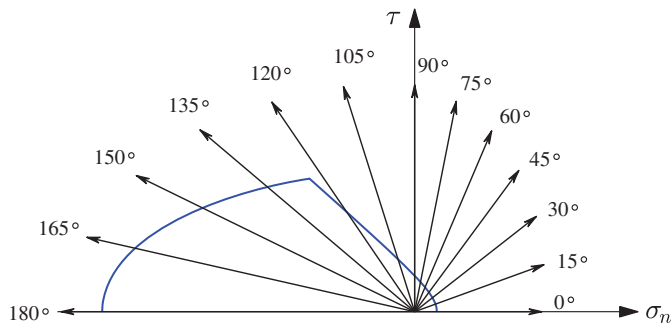

Fig. 4. Load paths used in the one-element test of the different constitutive models.

Table 1. Elastic properties of masonry units, joints, and potential cracks

Property	Value
Masonry units	
E_b (MPa)	16,700
υ	0.15
Joints	
k_n (N/mm^3)	82.00
k_s (N/mm^3)	36.00
Potential cracks	
k_n (N/mm^3)	10,000
k_s (N/mm^3)	10,000

Table 2. Inelastic properties for joints and potential cracks

Property	Joints	Potential cracks
Tension-shear failure criterion		
f_t (MPa)	0.25	2.0
G_f^I (N/mm)	0.018	0.008
C_0 (MPa)	$1.45f_t$	$1.45f_t$
C_{Q0} (MPa)	$50C_0$	C_0
$\tan\phi_0 / \tan\phi_r$	0.75/0.75	1.0/1.0
$\tan\psi_0 / \tan\psi_r$	0.001/0.0001	1.0/1.0
G_f^{II} (N/mm)	0.125	0.50
Compression cap failure criterion		
$\bar{\sigma}_0$ (MPa)	3.5	—
$\bar{\sigma}_p$ (MPa)	10.5	—
$\bar{\sigma}_m$ (MPa)	5.25	—
$\bar{\sigma}_r$ (MPa)	1.5	—
κ_p	0.09	—
κ_m	0.49	—

joints of a shear wall described by Vermeltfoort and Raijmakers (1993a, b) and given in Tables 1 and 2 were used in these one-element tests. The adaptive substepping algorithm was not activated in any of the considered constitutive models during these analyses to ensure a consistent (i.e., fixed) load step size for all constitutive models during each set of analyses. A total of 52 finite-element response simulations (corresponding to 13 load paths, each with 4 load step sizes) were carried out for each constitutive model, and these simulations were performed in ABAQUS with one CPU on a computer with an Intel Core i5-2400S 2.50 GHz processor and 12.0 GB RAM.

To determine the accuracy of the constitutive models, a base load step size corresponding to 1,000 relative displacement increments (i.e., N1000 with $|\Delta\mathbf{u}| = 2 \times 10^{-4}$ mm) was used to compare the results of the one-element tests. This load step size was considered sufficiently small to serve as an accurate reference solution for estimating the percentage error, δ, which is evaluated through the expression (Simo and Taylor 1986)

$$\delta = \frac{\sqrt{(\boldsymbol{\sigma}_n - \boldsymbol{\sigma}_{\text{exact}})^T \cdot (\boldsymbol{\sigma}_n - \boldsymbol{\sigma}_{\text{exact}})}}{\sqrt{\boldsymbol{\sigma}_{\text{exact}}^T \cdot \boldsymbol{\sigma}_{\text{exact}}}} \times 100 \qquad (13)$$

where $\boldsymbol{\sigma}_n$ = numerical traction response of the single interface element obtained by using different relative displacement increments; and $\boldsymbol{\sigma}_{\text{exact}}$ = reference solution of the traction response corresponding to the same constitutive model used to evaluate $\boldsymbol{\sigma}_n$ with 1,000 relative displacement increments (i.e., for N1000 load step sizes). The CPU time ratio (CTR) of the simulations for the different constitutive models with respect to the CPU time of the reference solution obtained using the CTSIM for each load path was also calculated. The results in terms of CTR and δ for the different constitutive models are reported in Tables 3 and 4 for the tension-shear region (load paths $\theta = 0°, 15°, 30°, 45°, 60°, 75°, 90°$) and the compression-shear region (load paths $\theta = 105°, 120°, 135°, 150°, 165°,$ and $180°$), respectively. Simulation results with percentage errors δ higher than 5% are bolded in these tables. Some simulations did not converge to a solution for large (fixed) load step sizes and are identified with a dash. As expected, the presented results indicate that the δ increased with decreasing CTR along all load paths for all constitutive models.

Table 3. CTR versus percentage error (δ) for tension-shear region

θ	N	CTSIM		Lourenco and Rots model		Macorini and Izzuddin model		Citto model	
		CTR	δ	CTR	δ	CTR	δ	CTR	δ
0	N100	0.093	<0.01	0.106	<0.01	0.106	2.62	**0.087**	**96.45**
	N50	0.050	<0.01	0.050	<0.01	**0.050**	**5.58**	**0.043**	**>100**
	N10	0.012	<0.01	0.012	<0.01	—	—	—	—
	N5	0.006	<0.01	0.006	<0.01	—	—	—	—
15	N100	0.099	<0.01	0.106	<0.01	0.113	2.26	0.134	1.67
	N50	0.042	<0.01	0.049	<0.01	0.049	4.81	**0.056**	**>100**
	N10	0.014	<0.01	0.021	<0.01	—	—	—	—
	N5	0.007	<0.01	0.007	0.02	—	—	—	—
30	N100	0.101	<0.01	0.101	<0.01	0.109	1.60	0.116	1.44
	N50	0.058	<0.01	0.051	<0.01	0.051	3.40	**0.051**	**>100**
	N10	0.014	<0.01	0.014	0.03	—	—	—	—
	N5	0.007	<0.01	0.007	0.04	—	—	—	—
45	N100	0.093	<0.01	0.099	<0.01	0.105	0.92	0.099	1.09
	N50	0.049	<0.01	0.062	<0.01	0.049	1.94	0.049	2.30
	N10	0.019	<0.01	0.019	<0.01	—	—	—	—
	N5	0.006	<0.01	**0.006**	**67.70**	—	—	—	—
60	N100	0.096	<0.01	0.110	<0.01	0.103	0.03	0.103	0.68
	N50	0.062	<0.01	0.062	<0.01	0.055	0.08	0.055	1.42
	N10	0.014	<0.01	0.021	<0.01	0.021	1.28	**0.014**	**>100**
	N5	0.007	<0.01	**0.007**	**>100**	—	—	—	—
75	N100	0.097	<0.01	0.090	<0.01	0.111	0.10	0.097	0.29
	N50	0.056	<0.01	0.049	<0.01	0.056	0.21	0.049	0.61
	N10	0.014	<0.01	0.014	<0.01	0.014	1.67	0.014	4.04
	N5	0.007	0.03	**0.007**	**37.87**	0.007	1.83	**0.007**	**10.16**
90	N100	0.097	0.42	0.103	0.02	0.109	0.35	0.085	0.22
	N50	0.048	0.87	0.048	0.04	0.055	0.72	0.042	0.46
	N10	0.012	3.42	0.012	0.33	0.018	3.50	0.018	2.60
	N5	**0.006**	**5.90**	0.006	1.46	**0.012**	**8.37**	0.006	4.58

Note: Bold values denote percentage errors $\delta > 5\%$.

Table 4. CTR versus percentage error (δ) for compression-shear region

θ	N	CTSIM		Lourenco and Rots model		Macorini and Izzuddin model		Citto model	
		CTR	δ	CTR	δ	CTR	δ	CTR	δ
105	N100	0.105	0.02	0.105	0.01	0.112	0.03	0.112	0.12
	N50	0.049	0.05	0.056	0.02	0.042	0.31	0.042	0.29
	N10	0.014	0.39	0.014	0.33	0.014	3.53	0.014	1.09
	N5	0.007	0.76	0.007	0.45	**0.007**	**10.39**	0.007	1.72
120	N100	0.101	0.06	0.109	0.06	0.109	0.05	**0.109**	**6.19**
	N50	0.051	0.12	0.065	0.13	0.051	0.11	**0.051**	**7.19**
	N10	0.014	1.17	0.014	1.31	0.014	3.16	**0.014**	**10.60**
	N5	**0.007**	**49.53**	**0.007**	**54.68**	0.007	73.19	0.007	>100
135	N100	0.102	0.07	0.102	0.08	0.102	0.11	0.109	0.57
	N50	0.054	0.14	0.048	0.16	0.048	0.24	0.051	1.23
	N10	0.014	1.32	0.014	1.54	0.014	0.60	**0.014**	**57.20**
	N5	**0.007**	**35.45**	**0.007**	**35.56**	**0.007**	**52.46**	0.007	>100
150	N100	0.094	0.05	0.101	0.07	0.081	0.12	0.107	0.65
	N50	0.054	0.11	0.054	0.14	0.047	0.24	0.040	1.34
	N10	0.013	1.03	0.013	1.26	0.013	2.24	**0.013**	**98.96**
	N5	**0.007**	**49.10**	**0.007**	**48.81**	—	—	—	—
165	N100	0.104	0.02	0.090	0.03	0.097	0.02	0.111	0.14
	N50	0.056	0.05	0.042	0.06	0.049	0.05	0.049	0.20
	N10	0.014	0.81	0.014	0.57	0.014	0.32	**0.021**	**11.19**
	N5	**0.007**	**55.63**	**0.007**	**54.73**	**0.007**	**61.02**	—	—
180	N100	0.097	<0.01	0.097	<0.01	0.103	0.01	0.097	1.18
	N50	0.055	<0.01	0.055	<0.01	0.055	0.02	0.055	2.10
	N10	0.014	<0.01	0.014	<0.01	0.014	0.22	**0.014**	**13.43**
	N5	**0.007**	**59.35**	**0.007**	**57.99**	—	—	—	—

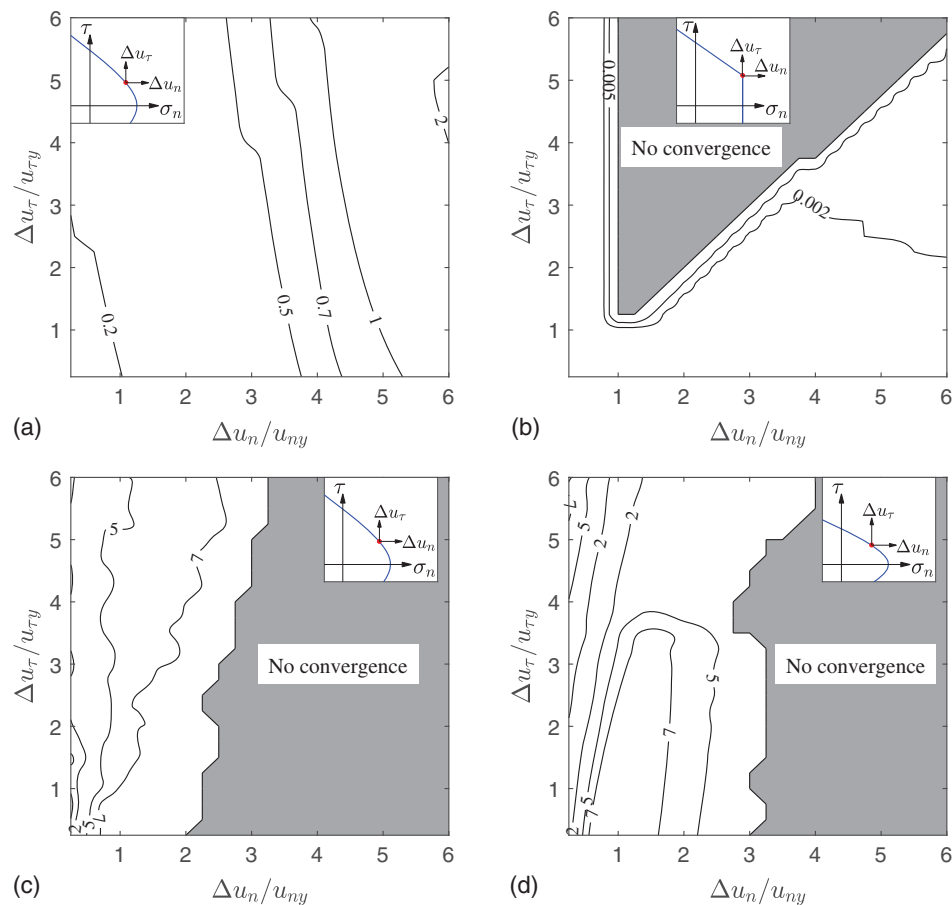Note: Bold values denote percentage errors $\delta > 5\%$.

Fig. 5. Isoerror maps for the point on the yield surfaces at $\theta = 36.13°$: (a) CTSIM; (b) Lourenco and Rots model; (c) Macorini and Izzuddin model; and (d) Citto model.

Tension-Shear Region

In the tension-shear region, 9 of 28 simulations did not converge for both the Macorini and Izzuddin and the Citto models, whereas all simulations for the CTSIM and the Lourenco and Rots model reached convergence for all load step sizes. Among the converged simulations, 27 simulations converged with less than 5% errors for the CTSIM (i.e., only 1 simulation had δ larger than 5%), 25 simulations converged with less than 5% errors for the Lourenco and Rots model (i.e., 3 simulations had δ larger than 5%), 17 simulations converged with less than 5% errors for the Macorini and Izzuddin model (i.e., 2 simulations had δ larger than 5% in addition to the 9 simulations that did not converge), and 13 simulations converged with less than 5% errors for the Citto model (i.e., 6 simulations had δ larger than 5% in addition to the 9 simulations that did not converge). Considering only the converged cases, the CPU time used by the simulation based on the CTSIM was less than or equal to the CPU time corresponding to the Lourenco and Rots, Macorini and Izzuddin, and Citto models in 25 of 28, 17 of 19, and 12 of 19 simulations, respectively.

The results presented in Table 3 for the tension-shear region indicate that the CTSIM is (1) computationally robust for all load step sizes except for Case N5 of load path $\theta = 90°$; (2) generally more accurate and computationally robust than the other three constitutive models considered here; and (3) computationally efficient, because for all considered load paths it can provide accurate results with load step sizes that are larger than or equal to those needed for any other constitutive models.

In order to understand better the mechanical differences among the different models, isoerror maps (Simo and Taylor 1986; De Borst and Feenstra 1990; Fuschi et al. 1992) were developed for all four constitutive models at the point on the yield surfaces corresponding to load path $\theta = 36.13°$ (Fig. 5). This point was selected as representative of the tension-shear region because it corresponds to the singularity point between the Rankine and Mohr–Coulomb failure criteria in the Lourenco and Rots model, and thus can be used to illustrate the advantages of using a single surface failure criterion by eliminating the singularity in the tension-shear region. The isoerror maps plot the error defined in Eq. (13) as a function of the normalized increment of relative displacement in the axial direction, u_n, and in the shear direction, u_τ. The normalization parameter for each of these relative displacement increments corresponds to the elastic relative displacement associated with the initial yielding in each of the two directions, respectively. Figs. 5(a–d) plot the isoerror maps for the CTSIM, Lourenco and Rots, Macorini and Izzuddin, and Citto models, respectively. The inset in each subfigure shows the location on the corresponding yield surface of the point selected as the origin of the isoerror map. The shaded region in each subfigure indicates the combinations of relative displacement increments for which the corresponding model cannot achieve convergence. Within the range of normalized relative displacement increments considered here, the CTSIM is the only model that can always achieve convergence. The Lourenco and Rots model does not converge within a region that corresponds approximately to $\Delta u_n / u_{ny} \geq 1$ and $\Delta u_\tau / u_{\tau y} \geq \Delta u_n / u_{ny}$. This result was first qualitatively observed by Lourenço (1994) and is due

both to the presence of a singularity in the yield surface and to the heuristic (i.e., trial-and-error) approach adopted in the Lourenco and Rots model to identify the active yield surface(s), which cannot guarantee convergence of the analysis for large load step sizes (Lourenço 1994). The Macorini and Izzuddin and the Citto models also present a region of nonconvergence, corresponding approximately to $\Delta u_n/u_{ny} \geq 2$ and $\Delta u_n/u_{ny} \geq 3$, respectively. This nonconvergence region for these two models is due to the presence of a non-physically meaningful branch of the yield surface having a quadratic functional form, as previously discussed. In particular, the convergence of these models is impaired as soon as the imposed relative displacement increment intercepts the non-physically meaningful branch of the corresponding yield surface. When the models converge, the magnitude of the errors is smallest for the Lourenco and Rots model (less than 0.01%), followed by the CTSIM (less than or equal to approximately 2%), and then by the Macorini and Izzuddin and the Citto models (less than 10%). These errors' magnitudes increase with the complexity of the functional form used for the corresponding yield surfaces (i.e., the Lourenco and Rots model is represented by linear yield functions, which correspond to the simplest functional form and the smallest percentage errors). The errors also depend on the hardening/softening hypothesis used in each model (i.e., the Macorini and Izzuddin and the Citto models use a work-hardening/softening hypothesis, which negatively affects the accuracy of their solutions compared with the results obtained using the CTSIM and the Lourenco and Rots model, which adopt a strain-hardening/softening hypothesis). Finally, the percentage error for all models is more sensitive to the size of the relative displacement increments in the axial direction than to that of the relative displacement increments in the shear direction. Based on these results, it is concluded that the CTSIM provides the best compromise between accuracy and robustness in the tension-shear region among all models considered in this study.

Compression-Shear Region

In the compression-shear region, 2 of 24 simulations did not converge for both the Macorini and Izzuddin and the Citto models, whereas all simulations for the CTSIM and the Lourenco and Rots model reached convergence. Among the converged simulations, 19 simulations converged with less than 5% errors for the CTSIM and the Lourenco and Rot model (i.e., 5 simulations had δ larger than 5%), 18 simulations converged with less than 5% errors for the Macorini and Izzuddin model (i.e., 4 simulations had δ larger than 5% in addition to the 2 simulations that did not converge), and 12 simulations converged with less than 5% errors for the Citto model (i.e., 9 simulations had δ larger than 5% in addition to the 3 simulations that did not converge). Considering only the converged cases, the CPU time used by the simulation based on the CTSIM was less than or equal to the CPU time corresponding to the Lourenco and Rots, Macorini and Izzuddin, and Citto models in 21 of 24, 16 of 22, and 18 of 22 simulations, respectively.

The results presented in Table 4 indicate that the performance of the CTSIM in the compression-shear region was practically identical to that of the Lourenco and Rots model because both models used the same compression cap model to represent the compression failure. These models are (1) computationally robust for all load step sizes except for the N5 (load paths $\theta = 120°$, $135°$, $150°$, $165°$, and $180°$) and N10 (load paths $\theta = 150°$ and $165°$); (2) more accurate and computationally robust than the Macorini and Izzuddin and the Citto models; and (3) computationally efficient, because both models provide accurate results with load step sizes that are larger than or equal to those for the Macorini and Izzuddin and Citto models.

Discussion of One-Element Test Results

The different performance of the constitutive models considered here can be more easily interpreted by analyzing the properties of the integration algorithm (i.e., the elastic predictor–plastic corrector strategy with local/global Newton–Raphson integration) and its interaction with the constitutive models' equations. During the plastic-corrector step, different sets of equations are solved in the different constitutive models depending upon which failure surface(s) is (are) violated, leading to different sizes of the Jacobian matrix that needs to be inverted. The size of this Jacobian matrix and the complexity of each Jacobian component both contribute toward the computational cost and accuracy of the different constitutive models in the different regions (i.e., tension, shear, and compression cap regions). For the CTSIM, three different cases can be encountered during the plastic-corrector step: (1) violation of the tension-shear failure surface, which involves a 6×6 Jacobian matrix [Eq. (14) in the Appendix]; (2) violation of the compression cap failure surface, which involves a 5×5 Jacobian matrix [Eq. (15) in the Appendix]; and (3) violation of both failure surfaces, which involves an 8×8 Jacobian matrix [Eq. (16) in the Appendix]. Fig. 6 illustrates the size of the Jacobian matrix used in the different regions of the different constitutive models.

The CTSIM is at least as efficient as the Lourenco and Rots model along load paths $\theta = 0°$, $15°$, $30°$, $45°$, and $60°$. In this region, the return mapping algorithm for the Lourenco and Rots model requires inverting a 3×3, 5×5, and/or 7×7 Jacobian matrix, depending on which failure surface(s) is (are) violated, whereas the CTSIM requires the inversion of a 6×6 Jacobian matrix. However, the Jacobian matrix for the Lourenco and Rots model mainly assumes a 7×7 dimension because, in most cases, both the Rankine and the Mohr–Coulomb failure surfaces are simultaneously violated, generally for large load steps or even for small load steps after the failure surfaces have experienced softening of their scalar parameters. The accuracy of the results obtained using the Lourenco and Rots model is very similar to or slightly lower than the accuracy of the CTSIM results for load paths $15°$, $30°$, $45°$, and $60°$ because the Lourenco and Rots model requires the solution of a multisurface plasticity problem (with a singularity located along the load path $\theta = 36.13°$ for the specific problem considered in this study), whereas the CTSIM uses a single surface in the same region. For load paths $\theta = 75°$ and $90°$, the Lourenco and Rots model is slightly more efficient than the CTSIM because the Jacobian matrix has dimensions 5×5 for the Lourenco and Rots model and 6×6 for the CTSIM. However, the CTSIM is consistently more accurate than the Lourenco and Rots model along these load paths, particularly for large load step sizes. In the shear-tension region, the Macorini and Izzuddin and the Citto models are very similar, because they use the same equation to define the failure surface and the hypothesis of work hardening. Compared with the CTSIM, the Macorini and Izzuddin and the Citto models perform poorly for load paths with small angles, i.e., $\theta \leq 60°$. These two models perform better for load paths $\theta = 75°$ and $90°$, and the Citto model is the most efficient and accurate model for $\theta = 90°$.

In the compression-shear region, both the CTSIM and the Lourenco and Rots model have a similar efficient and accurate behavior, with the exception of cases corresponding to large load step sizes. This is because in this region the two models use the same failure criteria. In the compression-shear region, the Macorini and Izzuddin and the Citto models are very different from each other and from the other constitutive models. In general, the Macorini and Izzudin model is more efficient than the CTSIM and the Lourenco and Rots model for small load step sizes, but is less
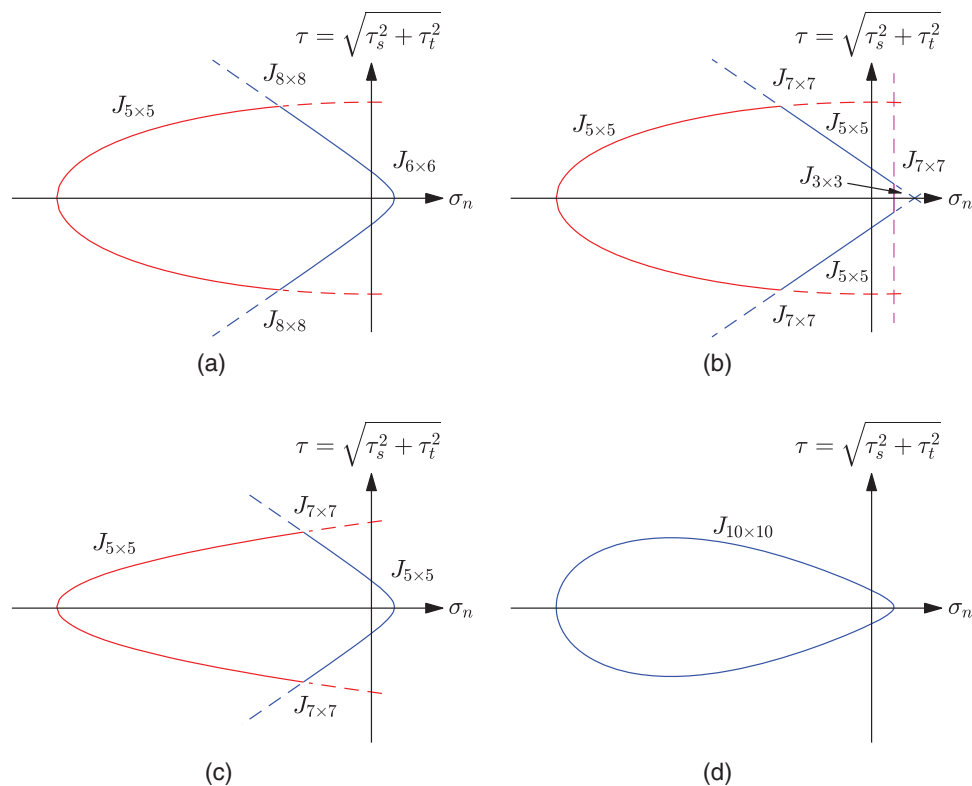
Fig. 6. Size of the Jacobian matrix for different regions of the constitutive models: (a) CTSIM; (b) Lourenco and Rots model; (c) Macorini and Izzuddin model; and (d) Citto model.

accurate (or lacks convergence) for large load step sizes. The Citto model generally performs poorly, both in terms of efficiency and accuracy. The efficiency of the Macorini and Izzuddin model for small load step sizes can be attributed to its evolution model for the compressive yield stress, which assumes a linear behavior up to the peak compressive yield stress, after which softening of the compressive yield stress takes place (Macorini and Izzuddin 2011). By contrast, the CTSIM and the Lourenco and Rots model assume a linear behavior only up to an initial compressive yield stress that is significantly lower than the peak compressive yield stress [e.g., approximately 1/3 of it for quasi-brittle materials (Bakeer 2009)], which is followed by hardening until the peak compressive yield stress and by softening afterward [Fig. 2 and Eq. (12)]. In addition, it appears that the lower accuracy of the Macorini and Izzuddin and the Citto models may be related to their use of the work-hardening hypothesis, in contrast to the CTSIM and the Lourenco and Rots model that use the hypothesis of strain hardening. In particular, for the specific problem considered in this paper of interface element constitutive models for masonry analysis based on the SMM approach, the hypothesis of strain hardening/softening appears to improve the robustness of the numerical response for yield surfaces that evolve for increasing plastic deformation, as assumed by the softening plasticity framework adopted in this study.

Constitutive Model Comparison Using Masonry Shear Wall Experimental Data

The performance of the proposed CTSIM was compared with the other constitutive models considered in this study through the numerical response analysis of an unreinforced masonry shear wall for which experimental data are available in Vermeltfoort and

Raijmakers (1993a, b). The numerical analyses were performed for all constitutive models using the FE software ABAQUS.

The masonry shear wall consisted of a pier with a width:height ratio approximately equal to 1, i.e., with dimensions $990 \times 1{,}000$ mm [Fig. 7(a)]. The wall was built using wire-cut solid clay blocks of dimensions $210 \times 52 \times 100$ mm and mortar layers 10 mm thick, and consisted of 18 courses of blocks, 2 of which (the bottom and top courses) were clamped to steel beams that were used to transfer the lateral load to the system [Fig. 7(a)]. The mortar was prepared with one part cement, two parts lime, and nine parts sand. The experimental test involved a uniformly distributed normal pressure ($p = 0.30$ MPa), followed by a monotonically increasing horizontal loading phase in which a horizontal displacement Δ was applied quasi-statically to the top of the wall through a steel beam while keeping the bottom boundary fixed horizontally. The material properties of blocks and mortar were obtained from experimental results of tension, shear, and compression tests reported by Vermeltfoort and Raijmakers (1993a, b) and are reported in Table 1 (elastic properties) and Table 2 (inelastic properties).

Definition of FE Models for Unreinforced Masonry Shear Wall

The SMM approach with elastic masonry units and nonlinear joints was adopted here for the FE modeling of the unreinforced masonry shear wall described previously. Plane stress conditions were assumed, and geometric nonlinearity [i.e., large strains and large displacements (Dassault Systèmes 2013)] was also included in the simulation of the FE models. The FE model consisted of a set of elastic masonry units bonded by potential crack, potential slip, and crushing planes at joints [Fig. 7(b)]. To model the cracking
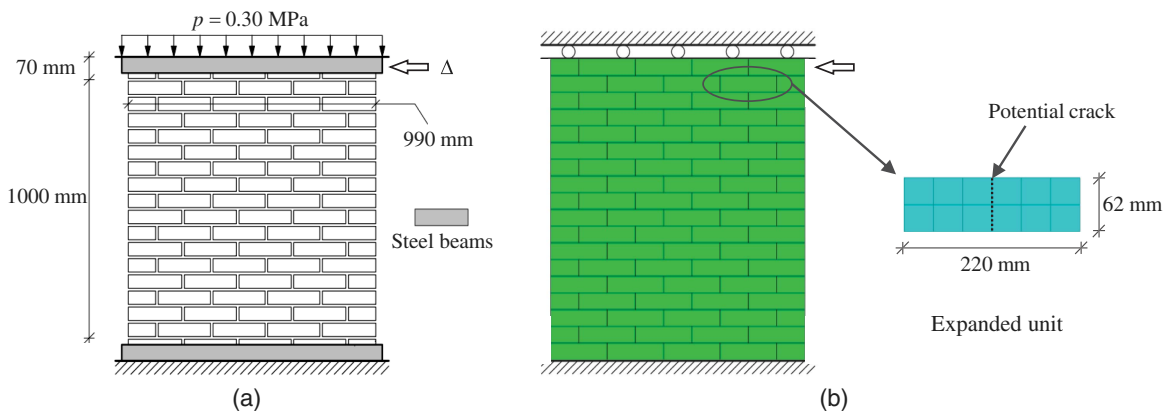
Fig. 7. Masonry shear walls: (a) shear walls; and (b) SMM used for simulating the shear wall.

of the masonry units, a potential crack was placed vertically in the middle of each unit [Fig. 7(b)]. All the degrees of freedoms were restrained at the bottom of the FE model, and a monotonically increasing horizontal displacement was applied on the side of the top course of the FE model while keeping the top edge of the FE model vertically fixed (Fig. 7). A general procedure for static loading based on an incremental-iterative globally convergent Newton–Raphson method with the line search technique was used in ABAQUS to solve the nonlinear system of equilibrium equations for the different FE models (Dassault Systèmes 2013). In addition, an automatic load step increment technique was adopted for efficient and robust simulation of the response of the different FE models with initial, minimum, and maximum normalized increment sizes equal to 1×10^{-4}, 1×10^{-9}, and 5×10^{-4}, respectively.

In the FE models of the masonry shear wall, the masonry units were modeled using a four-node bilinear plane stress quadrilateral element with reduced integration and hourglass control [CPS4R element (Dassault Systèmes 2013)], and the joints and potential cracks were modeled by using a four-node two-dimensional cohesive element [COH2D4 element (Dassault Systèmes 2013)]. A mesh sensitivity analysis of the FE Model was performed to ensure a good compromise between accuracy and computational costs for all the constitutive models. The mesh used in this study consisted of six interface elements employed for each bed joint (i.e., three interface elements for the bed joint of each half masonry unit), two interface elements employed for each head joint and for potential vertical cracks, and six CPS4R elements for each half masonry unit. One FE model was built for each of the constitutive models considered in this study, i.e., the CTSIM, Lourenco and Rots, Macorini and Izzuddin, and Citto models. The adaptive substepping algorithm was activated for all considered constitutive models to achieve maximum computational efficiency in all FE analyses. The behavior of the potential vertical cracks did not include the compression failure mechanism. Thus, the compression failure surface of the CTSIM, Lourenco and Rots model, and Macorini and Izzuddin model was deactivated for the interface element of potential vertical cracks, and a high dummy value in the Citto model was used for the compressive yield stress to avoid activation of the failure surface in the compression region of this constitutive model.

Comparison of FE Responses and Experimental Data

The experimental load-displacement curves with their numerical counterparts for all constitutive models are compared in Fig. 8. The FE response results obtained using any of the interface element constitutive models considered in this study were in very good

agreement with the experimental behavior, with a ratio of the numerically simulated peak load to the average experimental peak load equal to 1.04, 1.01, 1.10, and 0.98 for the CTSIM, Lourenco and Rots, Macorini and Izzuddin, and Citto models, respectively. The deformed shape and the minimum principal stress distribution (corresponding to the maximum compressive stress) at an applied top horizontal displacement $\Delta = 4$ mm (i.e., the maximum displacement recorded in the experimental tests) of the FE analyses using different constitutive models are presented in Fig. 9. For the sake of visualization, the interface elements are represented by empty spaces in this figure so that highly plasticized interface elements appear as openings between masonry units. The stress distributions of the shear wall FE models corresponding to the different constitutive models were very similar. In addition, the crack patterns were also similar to those observed experimentally for all FE models, except for that corresponding to the Citto model. During the application of the monotonically increasing horizontal load, horizontal tensile cracks developed at the bottom and top of the wall, particularly in the bed joint at an early loading stage, followed by the formation of a diagonal stepped crack due to a combined tension-shear failure of the joints. For large horizontal load levels, the diagonal stepped crack was followed by crushing of the toes of the masonry and tensile cracking within the masonry units, leading to the overall failure of the masonry wall. The cracking of the masonry units was significant for all constitutive models except
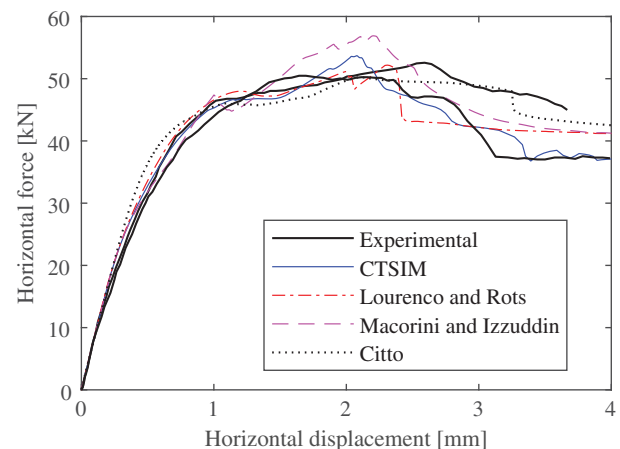

Fig. 8. Comparison of experimental and numerical results in terms of load-displacement response of the shear wall.
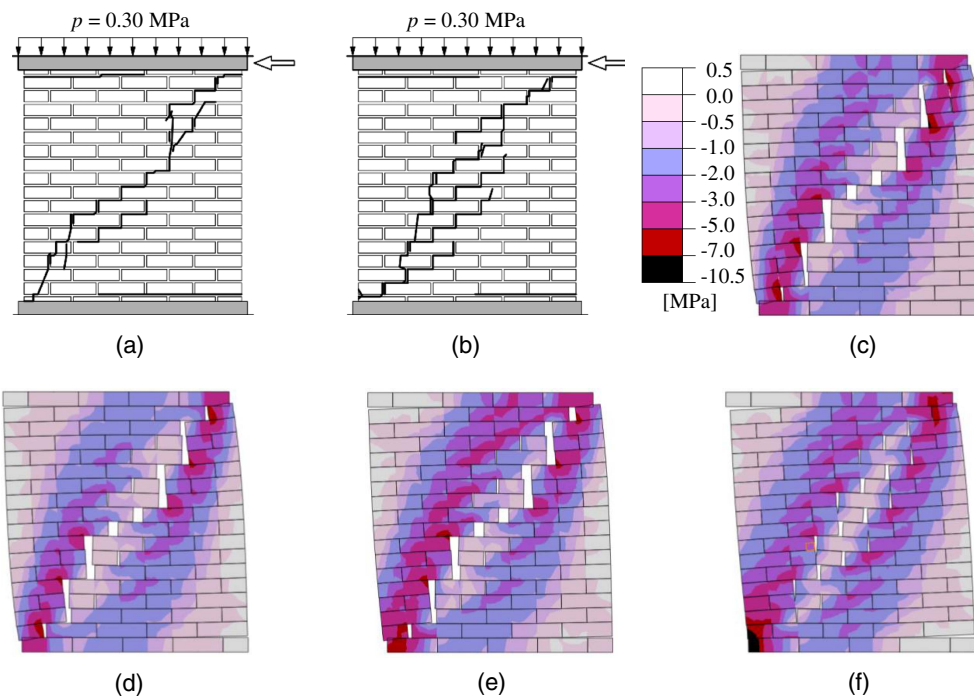
Fig. 9. Comparison of experimental and numerical results: (a and b) experimental crack patterns for the two specimens; (c) deformed shape and distribution of minimum principal stress for CTSIM; (d) deformed shape and distribution of minimum principal stress for Lourenco and Rots model; (e) deformed shape and distribution of minimum principal stress for Macorini and Izzuddin model; and (f) deformed shape and distribution of minimum principal stress for Citto model.

Table 5. Load increments and CTR for different constitutive models in the analysis of the benchmark masonry shear wall

Item	CTSIM	Lourenco and Rots model	Macorin and Izzuddin model	Citto model
Increments	26,620	29,679	35,564	40,119
Cutbacks	6,796	7,861	9,538	11,137
Total iterations	106,567	114,378	136,680	170,495
CTR	1.00	1.37	1.22	1.48

the Citto model, in which the behavior of the potential vertical crack within a unit was more ductile than for the other constitutive models, leading to smaller crack's openings. This behavior was due to the use of a high dummy value for the compressive yield stress of cracks within the masonry units, which was required to avoid the activation of the compressive failure surface in the Citto model. In fact, whereas for the CTSIM, Lourenco and Rots, and Macorini and Izzuddin models the compressive failure surface is independent of the tension-shear behavior, a change of the compressive yield stress in the Citto model also affects the shape of the failure surface in the tension-shear region. This shape change deteriorates the capability of the Citto model to simulate the brittle cracking of masonry units.

Assessment of Computational Cost

The FE models corresponding to the different constitutive models were also compared in terms of computational cost. In particular, Table 5 reports the number of increments, cutbacks (reduction of load/displacement increment size when the iterative global solution algorithm cannot converge within a specified number of iterations), and total iterations (Dassault Systèmes 2013), as well as the CTRs corresponding to the FE analyses for each of the considered

constitutive models. The CTRs were calculated with respect to the total CPU time corresponding to the FE analysis using the CTSIM, which was assumed as a reference with CTR = 1.00. The FE analysis based on the CTSIM took 9.53 h of CPU time using an Intel Core i5-2400S 2.50 GHz processor and 12.0 GB RAM. The FE analysis using the CTSIM was found to be the least computationally expensive among those considered in this study. The second most computationally efficient model was the Macorini and Izzuddin model, with CTR = 1.22, followed by the Lourenco and Rots model (CTR = 1.37) and the Citto model (CTR = 1.48). Moreover, the CTSIM completed the simulation with the smallest numbers of increments, cutbacks, and total iterations. This result indicates that the CTSIM can allow FE simulation of the masonry shear wall with larger load steps than those of the other interface element constitutive models, which explains the lower computational cost of the proposed constitutive model.

Table 6 reports the number of the local iterations corresponding to the different regions of constitutive models during the FE simulations of the benchmark masonry shear wall. The CTSIM required the least number of local iterations, 21.15 million, followed by the Macorini and Izzuddin (24.77 million), Lourenco and Rots (27.68 million), and Citto models (29.81 million).

The FE simulation with the CTSIM required 17.96 million local iterations (out of 21.15 million) occurring in the tension and shear failure region, which corresponds to a 6×6 Jacobian matrix. For the Lourenco and Rots model, 24.58 million local iterations (out of 27.68 million) occurred in the same failure region. These local iterations were associated with three different failure conditions: (1) violation of the Rankine failure criterion, which requires the inversion of a 3×3 Jacobian matrix (0.52 million iterations); (2) violation of the Mohr–Coulomb failure criterion, which requires the inversion of a 5×5 Jacobian matrix (18.47 million iterations); and (3) violation of both failure criteria simultaneously (T-S corner),

Table 6. Number of iterations under different conditions for different models

Violation of failure criterion	CTSIM		Lourenco and Rots model		Macorini and Izzuddin model		Citto model	
	Iterations (millions)	%	Iterations (millions)	%	Iterations (millions)	%	Iterations (millions)	%
Rankine	—	—	0.52	1.89	—	—	29.81	100
Mohr–Coulomb	—	—	18.47	66.74	—	—		
Tension-shear	17.96	82.60	—	—	24.42	98.58		
Compression cap	3. 01	16.58	2.93	10.58	0.32	1.31		
T-S corner[a]	—	—	5.59	20.19	—	—		
S-C corner[b]	0.18	0.82	0.17	0.60	0.03	0.11		
Total	21.15		27.68		24.77		29.81	

[a]Multisurface singularity between Rankine and Mohr–Coulomb failure criterion.

[b]Multisurface singularity between Mohr–Coulomb or tension-shear and compression cap failure criterion.

which requires the inversion of a 7×7 Jacobian matrix (5.59 million iterations). Comparing the FE simulations with the CTSIM and the Lourenco and Rots model showed that the use of a smooth failure surface instead of the two different failure surfaces (the Rankine and Mohr–Coulomb failure surfaces) resulted in 6.62 million fewer local iterations. Although the computational cost associated with each local iteration for the two constitutive models was different (generally lower for the Lourenco and Rots model), the CTSIM resulted in lower CPU times because of the significantly smaller number of iterations required. Therefore, it was concluded that the use of smooth failure surface to describe the shear and tension failure region results in a more computationally efficient interface element constitutive model. Furthermore, the FE simulation with the Macorini and Izzuddin model required 24.42 million local iterations violating the tension and shear failure criterion, which was 6.46 million iterations more (approximately 35.97%) than the corresponding total local iterations for the CTSIM. In addition, the FE simulation with the Macorini and Izzuddin model required a comparatively higher number of global increments (approximately 33.60% higher) than did the CTSIM (Table 5). The higher number of local iterations and global increments may be due to the fact that the Macorini and Izzuddin model requires smaller load step sizes to achieve the same accuracy as the CTSIM, as shown by the results reported for the one-element test.

In the compression cap failure region, the FE simulations of the masonry shear wall with the CTSIM and the Lourenco and Rots model resulted in 3.19 million and 3.10 million local iterations, respectively, which required the inversion of a 5×5 Jacobian matrix. Thus, the Lourenco and Rots model was slightly more efficient than the CTSIM in the compression cap failure region. The Macorini and Izzuddin model required only 0.35 million local iterations that corresponded to violating the compression failure surface. This difference in the number of local iterations compared with the CTSIM and the Lourenco and Rots model was mainly due to the different assumptions for the evolution of the compressive yield stress and the different values for the initial compressive yield stress. In fact, these different assumptions resulted in the Macorini and Izzuddin model exhibiting linear elastic behavior for a much wider range of strains and stresses compared with the CTSIM and the Lourenco and Rots model.

The FE simulation of the masonry shear wall with the Citto model resulted in the largest number of local iterations, 26.81 million local iterations, compared with the other constitutive models. Thus, the Citto model was the least efficient model among those considered in this study for simulating the response of this masonry shear wall. This result was due to (1) the lower accuracy in normal and shear stress evaluations for a given load/displacement step size (as shown by the results reported for the one-element test); (2) the larger size of the Jacobian matrix (10×10) that needs to be

inverted in the local iterations; and (3) the more-complex equation used for representation of the single failure surface. The comparison of the computational costs of the FE simulations corresponding to the different constitutive models considered in this study (i.e., the CTSIM, Lourenco and Rots model, Macorini and Izzuddin model, and Citto model) indicates that the use of a single failure surface for all failure modes decreases the overall computational efficiency of the interface element constitutive model.

Conclusions

A new interface element constitutive model, the coupled tension-shear interface model (CTSIM), was proposed in this paper for finite-element analysis of masonry using the simplified micromodeling approach. This new model is capable of simulating tension cracking, shear slipping, and compression failure, and is defined by a convex composite failure surface consisting of a tension-shear failure criterion and a compression cap failure criterion. The constitutive model is implemented in the FE software ABAQUS through a user-defined material subroutine. The different constitutive equations of the CTSIM are integrated using the implicit backward Euler integration method, and the integrated equations are solved monolithically with the local/global Newton–Raphson technique, which leads to a combined local and global solution strategy. Moreover, the CTSIM is combined with an adaptive substepping strategy to ensure convergence and accuracy of the final solution for larger load step sizes.

The performance of the CTSIM was assessed through a series of one-element tests and through the comparison of FE response simulations and experimental results for an unreinforced shear wall. Furthermore, the robustness, computational cost, and accuracy of the CTSIM were also compared with three constitutive models available in the literature, i.e., the Lourenco and Rots, Macorini and Izzuddin, and Citto models. The comparison of one-element test results showed that the CTSIM is at least as efficient as and generally more robust than the other constitutive models for varying load step sizes and load paths. The comparison of the FE results for the masonry shear wall indicated that the CTSIM is more efficient than and at least as accurate as the other constitutive models. Moreover, it was concluded that (1) the use of a single failure surface for Mode-I and Mode-II failure can improve the computational efficiency and robustness of the constitutive model compared with constitutive models that use two separate failure surfaces; (2) the use of a single failure surface for all failure mechanisms has negative effects on the computational efficiency and robustness of the constitutive model compared with constitutive models that use multisurface criteria; and (3) constitutive models based on the hypothesis of strain hardening seem to be more efficient and robust than those based on the hypothesis of work hardening.

Appendix. Integration Scheme for Constitutive Equations

The local/global Newton–Raphson strategy (Ottosen and Ristinmaa 2005; Caballero et al. 2008; Macorini and Izzuddin 2011) is used to solve the nonlinear system of algebraic equations obtained from the implicit backward Euler integration (Simo and Hughes 2006) of the CTSIM. This integration procedure leads to a set of algebraic-incremental equations that are solved using an elastic predictor-plastic corrector approach. The plastic correction step is performed when the trial stress violates at least one failure criteria (failure surfaces) and consists of an iteration process that requires

(1) evaluating the residuals of the nonlinear constitutive equations, (2) evaluating the Jacobian of the residuals, (3) solving the set of algebraic equations to obtain the increments of the independent variables, and (4) evaluating the updated residuals and repeating the iteration until these residuals become smaller than a specified tolerance. Three different cases can occur in the plastic correction step: (1) violation of the tension-shear failure criterion, (2) violation of the compression cap failure criterion, and (3) violation of both tension-shear and compression cap failure criteria. The Jacobians of the residuals for these three cases are

1. Violation of the tension-shear failure criterion, with independent variables $\boldsymbol{\sigma}$, κ_1, κ_2, and $\Delta\lambda_1$

$$
\mathbf{J}(\boldsymbol{\sigma}, \kappa_1, \kappa_2, \Delta\lambda_1) = \begin{bmatrix} \mathbf{I}_3 + \mathbf{k} \cdot \Delta\lambda_1 \cdot \dfrac{\partial^2 Q_1}{\partial \boldsymbol{\sigma}^2} & \mathbf{k} \cdot \Delta\lambda_1 \cdot \dfrac{\partial^2 Q_1}{\partial \kappa_1 \partial \boldsymbol{\sigma}} & \mathbf{k} \cdot \Delta\lambda_1 \cdot \dfrac{\partial^2 Q_1}{\partial \kappa_2 \partial \boldsymbol{\sigma}} & \mathbf{k} \cdot \dfrac{\partial Q_1}{\partial \boldsymbol{\sigma}} \\ -\dfrac{\partial \Delta\kappa_1}{\partial \boldsymbol{\sigma}} & 1 - \dfrac{\partial \Delta\kappa_1}{\partial \kappa_1} & -\dfrac{\partial \Delta\kappa_1}{\partial \kappa_2} & -\dfrac{\partial \Delta\kappa_1}{\partial \lambda_1} \\ -\dfrac{\partial \Delta\kappa_2}{\partial \boldsymbol{\sigma}} & -\dfrac{\partial \Delta\kappa_2}{\partial \kappa_1} & 1 - \dfrac{\partial \Delta\kappa_2}{\partial \kappa_2} & -\dfrac{\partial \Delta\kappa_2}{\partial \lambda_1} \\ \dfrac{\partial F_1}{\partial \boldsymbol{\sigma}} & \dfrac{\partial F_1}{\partial \kappa_1} & \dfrac{\partial F_1}{\partial \kappa_2} & 0 \end{bmatrix}_{6\times6} \tag{14}
$$

where $\mathbf{I}_3 = 3 \times 3$ identity matrix; and $\Delta\lambda_1$ = increment of the plastic multiplier for the tension-shear failure surface $F_1(\boldsymbol{\sigma}, \kappa_1, \kappa_2)$.

2. Violation of the compression cap failure criterion, with independent variables $\boldsymbol{\sigma}$, κ_3, and $\Delta\lambda_2$

$$
\mathbf{J}(\boldsymbol{\sigma}, \kappa_3, \Delta\lambda_2) = \begin{bmatrix} \mathbf{I}_3 + \mathbf{k} \cdot \Delta\lambda_2 \cdot \dfrac{\partial^2 F_2}{\partial \boldsymbol{\sigma}^2} & \mathbf{k} \cdot \Delta\lambda_2 \cdot \dfrac{\partial^2 F_2}{\partial \kappa_3 \partial \boldsymbol{\sigma}} & \mathbf{k} \cdot \dfrac{\partial F_2}{\partial \boldsymbol{\sigma}} \\ -\dfrac{\partial \Delta\kappa_3}{\partial \boldsymbol{\sigma}} & 1 - \dfrac{\partial \Delta\kappa_3}{\partial \kappa_3} & -\dfrac{\partial \Delta\kappa_3}{\partial \lambda_2} \\ \dfrac{\partial F_2}{\partial \boldsymbol{\sigma}} & \dfrac{\partial F_2}{\partial \kappa_3} & 0 \end{bmatrix}_{5\times5} \tag{15}
$$

where $\Delta\lambda_2$ = increment of the plastic multiplier for the compression cap failure surface $F_2(\boldsymbol{\sigma}, \kappa_3)$.

3. Violation of both tension-shear and compression cap failure criteria (S-C corner), with independent variables $\boldsymbol{\sigma}$, κ_1, κ_2, κ_3, $\Delta\lambda_1$, and $\Delta\lambda_2$

$$
\mathbf{J}(\boldsymbol{\sigma}, \boldsymbol{\kappa}, \Delta\lambda_1, \Delta\lambda_2) = \begin{bmatrix} \mathbf{I}_3 + \boldsymbol{k} \cdot \Delta\lambda_1 \cdot \dfrac{\partial^2 Q_1}{\partial \boldsymbol{\sigma}^2} + \mathbf{k} \cdot \Delta\lambda_2 \cdot \dfrac{\partial^2 F_2}{\partial \boldsymbol{\sigma}^2} & \mathbf{k} \cdot \Delta\lambda_1 \cdot \dfrac{\partial^2 Q_1}{\partial \boldsymbol{\kappa} \partial \boldsymbol{\sigma}} + \mathbf{k} \cdot \Delta\lambda_2 \cdot \dfrac{\partial^2 F_2}{\partial \boldsymbol{\kappa} \partial \boldsymbol{\sigma}} & \mathbf{k} \cdot \dfrac{\partial Q_1}{\partial \boldsymbol{\sigma}} & \mathbf{k} \cdot \dfrac{\partial F_2}{\partial \boldsymbol{\sigma}} \\ -\dfrac{\partial \Delta\boldsymbol{\kappa}}{\partial \boldsymbol{\sigma}} & \boldsymbol{I}_3 - \dfrac{\partial \Delta\boldsymbol{\kappa}}{\partial \boldsymbol{\kappa}} & -\dfrac{\partial \Delta\boldsymbol{\kappa}}{\partial \lambda_1} & -\dfrac{\partial \Delta\boldsymbol{\kappa}}{\partial \lambda_2} \\ \dfrac{\partial F_1}{\partial \boldsymbol{\sigma}} & \dfrac{\partial F_1}{\partial \boldsymbol{\kappa}} & 0 & 0 \\ \dfrac{\partial F_2}{\partial \boldsymbol{\sigma}} & \dfrac{\partial F_2}{\partial \boldsymbol{\kappa}} & 0 & 0 \end{bmatrix}_{8\times8} \tag{16}
$$

where $\boldsymbol{\kappa} = \{\kappa_1, \kappa_2, \kappa_3\}^T$. Some of the terms in Eqs. (14)–(16) are matrixes or vectors.

Acknowledgments

References

Abbo, A., and S. Sloan. 1995. "A smooth hyperbolic approximation to the Mohr-Coulomb yield criterion." *Comput. Struct.* 54 (3): 427–441. https://doi.org/10.1016/0045-7949(94)00339-5.

Anand, S. C., and K. K. Yalamanchili. 1996. "Three-dimensional failure analysis of composite masonry walls." *J. Struct. Eng.* 122 (9): 1031–1039. https://doi.org/10.1061/(ASCE)0733-9445 (1996)122:9(1031).

Andreaus, U. 1996. "Failure criteria for masonry panels under in-plane loading." *J. Struct. Eng.* 122 (1): 37–46. https://doi.org/10.1061/(ASCE)0733-9445(1996)122:1(37).

Aref, A. J., and K. M. Dolatshahi. 2013. "A three-dimensional cyclic meso-scale numerical procedure for simulation of unreinforced masonry structures." *Comput. Struct.* 120: 9–23. https://doi.org/10.1016/j.compstruc.2013.01.012.

Atkinson, R., B. Amadei, S. Saeb, and S. Sture. 1989. "Response of masonry bed joints in direct shear." *J. Struct. Eng.* 115 (9): 2276–2296. https://doi.org/10.1061/(ASCE)0733-9445(1989)115:9(2276).

Bakeer, T. T. 2009. *Collapse analysis of masonry structures under earthquake actions*. Dresden, Germany: TU Dresden.

Bathe, K.-J. 2006. *Finite element procedures*. Watertown, MA: Klaus-Jurgen Bathe.

Caballero, A. 2005. "3D meso-mechanical numerical analysis of concrete fracture using interface elements." Ph.D. dissertation, Dept. of Geotechnical Engineering and Geosciences, Polytechnic Univ. of Catalonia.

Caballero, A., K. Willam, and I. Carol. 2008. "Consistent tangent formulation for 3D interface modeling of cracking/fracture in quasi-brittle materials." *Comput. Methods Appl. Mech. Eng.* 197 (33): 2804–2822. https://doi.org/10.1016/j.cma.2008.01.011.

Chaimoon, K., and M. M. Attard. 2007. "Modeling of unreinforced masonry walls under shear and compression." *Eng. Struct.* 29 (9): 2056–2068. https://doi.org/10.1016/j.engstruct.2006.10.019.

Chisari, C., L. Macorini, C. Amadio, and B. A. Izzuddin. 2015. "An inverse analysis procedure for material parameter identification of mortar joints in unreinforced masonry." *Comput. Struct.* 155: 97–105. https://doi.org/10.1016/j.compstruc.2015.02.008.

Chisari, C., L. Macorini, C. Amadio, and B. A. Izzuddin. 2018. "Identification of mesoscale model parameters for brick-masonry." *Int. J. Solids Struct.* 146: 224–240. https://doi.org/10.1016/j.ijsolstr.2018.04.003.

Citto, C. 2008. "Two-dimensional interface model applied to masonry structures." M.S. thesis, Dept. of Civil, Environmental and Architectural Engineering, Univ. of Colorado Boulder.

Cuellar-Azcarate, M. C. 2016. "Engineered earthen masonry structures for extreme wind loads." Ph.D. dissertation, Dept. of Civil and Environmental Engineering, Univ. of South Carolina.

da Porto, F., G. Guidi, E. Garbin, and C. Modena. 2010. "In-plane behavior of clay masonry walls: Experimental testing and finite-element modeling." *J. Struct. Eng.* 136 (11): 1379–1392. https://doi.org/10.1061/(ASCE)ST.1943-541X.0000236.

Dassault Systèmes. 2013. "Abaqus 6.13 documentation." In *Abaqus analysis user's guide*. Providence, RI: Dassault Systèmes.

De Borst, R., and P. H. Feenstra. 1990. "Studies in anisotropic plasticity with reference to the Hill criterion." *Int. J. Numer. Methods Eng.* 29 (2): 315–336. https://doi.org/10.1002/nme.1620290208.

Dhanasekar, M., P. W. Kleeman, and A. W. Page. 1985. "Biaxial stress-strain relations for brick masonry." *J. Struct. Eng.* 111 (5): 1085–1100. https://doi.org/10.1061/(ASCE)0733-9445(1985)111:5(1085).

Dolatshahi, K. M., and A. J. Aref. 2011. "Two-dimensional computational framework of meso-scale rigid and line interface elements for masonry structures." *Eng. Struct.* 33 (12): 3657–3667. https://doi.org/10.1016/j.engstruct.2011.07.030.

Furukawa, A., R. Spence, Y. Ohta, and E. So. 2010. "Analytical study on vulnerability functions for casualty estimation in the collapse of adobe buildings induced by earthquake." *Bull. Earthquake Eng.* 8 (2): 451–479. https://doi.org/10.1007/s10518-009-9156-z.

Fuschi, P., D. Perić, and D. Owen. 1992. "Studies on generalized midpoint integration in rate-independent plasticity with reference to plane stress J_2-flow theory." *Comput. Struct.* 43 (6): 1117–1133. https://doi.org/10.1016/0045-7949(92)90012-O.

Gambarotta, L., and S. Lagomarsino. 1997a. "Damage models for the seismic response of brick masonry shear walls. Part I: The mortar joint model and its applications." *Earthquake Eng. Struct. Dyn.* 26 (4): 423–439. https://doi.org/10.1002/(SICI)1096-9845(199704)26:4<423::AIDEQE650>3.0.CO;2-%23.

Gambarotta, L., and S. Lagomarsino. 1997b. "Damage models for the seismic response of brick masonry shear walls. Part II: The continuum model and its applications." *Earthquake Eng. Struct. Dyn.* 26 (4): 441–462. https://doi.org/10.1002/(SICI)1096-9845(199704)26:4<441::AID-EQE651>3.0.CO;2-0.

Giambanco, G., and L. Di Gati. 1997. "A cohesive interface model for the structural mechanics of block masonry." *Mech. Res. Commun.* 5 (24): 503–512. https://doi.org/10.1016/S0093-6413(97)00055-4.

Giambanco, G., S. Rizzo, and R. Spallino. 2001. "Numerical analysis of masonry structures via interface models." *Comput. Methods Appl. Mech. Eng.* 190 (49): 6493–6511. https://doi.org/10.1016/S0045-7825(01)00225-0.

Goodman, R. E., R. L. Taylor, and T. L. Brekke. 1968. "A model for the mechanics of jointed rocks." *J. Soil Mech. Found. Div.* 94 (3): 637–660.

Greco, F., L. Leonetti, R. Luciano, and P. Trovalusci. 2017. "Multiscale failure analysis of periodic masonry structures with traditional and fiber-reinforced mortar joints." *Composites Part B* 118: 75–95. https://doi.org/10.1016/j.compositesb.2017.03.004.

Khisamitov, I., and G. Meschke. 2018. "Variational approach to interface element modeling of brittle fracture propagation." *Comput. Methods Appl. Mech. Eng.* 328: 452–476. https://doi.org/10.1016/j.cma.2017.08.031.

Kumar, N., A. Rajagopal, and M. Pandey. 2014a. "A rate independent cohesive zone model for modeling failure in quasi-brittle materials." *Mech. Adv. Mater. Struct.* 22 (8): 681–696. https://doi.org/10.1080/15376494.2013.855852.

Kumar, N., A. Rajagopal, and M. Pandey. 2014b. "Plasticity based approach for failure modelling of unreinforced masonry." *Eng. Struct.* 80: 40–52. https://doi.org/10.1016/j.engstruct.2014.08.021.

Lotfi, H. R., and P. B. Shing. 1991. "An appraisal of smeared crack models for masonry shear wall analysis." *Comput. Struct.* 41 (3): 413–425. https://doi.org/10.1016/0045-7949(91)90134-8.

Lotfi, H. R., and P. B. Shing. 1994. "Interface model applied to fracture of masonry structures." *J. Struct. Eng.* 120 (1): 63–80. https://doi.org/10.1061/(ASCE)0733-9445(1994)120:1(63).

Lourenco, P. B., and J. G. Rots. 1997. "Multisurface interface model for analysis of masonry structures." *J. Eng. Mech.* 123 (7): 660–668. https://doi.org/10.1061/(ASCE)0733-9399(1997)123:7(660).

Lourenço, P. B. 1994. *Analysis of masonry structures with interface elements: Theory and applications*. Rep. No. 03-21-22-0-01. Delft, Netherlands: Delft Univ. of Technology.

Lourenço, P. B. 1996. "Computational strategies for masonry structures." Ph.D. dissertation, Dept. of Civil Engineering, Delft Univ. of Technology.

Macorini, L., and B. Izzuddin. 2011. "A non-linear interface element for 3D mesoscale analysis of brick-masonry structures." *Int. J. Numer. Methods Eng.* 85 (12): 1584–1608. https://doi.org/10.1002/nme.3046.

Metcalf, M., J. Reid, and M. Cohen. 2011. *Modern Fortran explained (numerical mathematics and scientific computation)*. New York: Oxford University Press.

Miccoli, L., A. Garofano, P. Fontana, and U. Müller. 2015. "Experimental testing and finite element modelling of earth block masonry." *Eng. Struct.* 104: 80–94. https://doi.org/10.1016/j.engstruct.2015.09.020.

Minga, E., L. Macorini, and B. A. Izzuddin. 2018. "A 3D mesoscale damage-plasticity approach for masonry structures under cyclic loading." *Meccanica* 53 (7): 1591–1611. https://doi.org/10.1007/s11012-017-0793-z.

Oliveira, D. V., and P. B. Lourenço. 2004. "Implementation and validation of a constitutive model for the cyclic behaviour of interface elements." *Comput. Struct.* 82 (17): 1451–1461. https://doi.org/10.1016/j.compstruc.2004.03.041.

Ottosen, N. S., and M. Ristinmaa. 2005. *The mechanics of constitutive modeling*. Amsterdam, Netherlands: Elsevier.

Page, A. W. 1978. "Finite element model for masonry." *J. Struct. Div.* 104 (8): 1267–1285.

Page, A. W. 1983. "The strength of brick masonry under biaxial tension-compression." *Int. J. Masonry Constr.* 3 (1): 26–31.

Pelà, L. 2009. "Continuum damage model for nonlinear analysis of masonry structures." Ph.D. dissertation, Dept. of Strength of Materials and Structural Engineering, Polytechnic Univ. of Catalonia.

Pérez-Foguet, A., A. Rodríguez-Ferran, and A. Huerta. 2001. "Consistent tangent matrices for substepping schemes." *Comput. Methods Appl.*

Mech. Eng. 190 (35–36): 4627–4647. https://doi.org/10.1016/S0045-7825(00)00336-4.

Rots, J. G., and B. Picavet. 1997. *Structural masonry: An experimental/numerical basis for practical design rules*. Rotterdam, Netherlands: A.A. Balkema.

Schellekens, J. C. J. 1992. "Computational strategies for composite structures." Ph.D. dissertation, Dept. of Civil Engineering and Geosciences, Delft Univ. of Technology.

Shing, P. B., and T. Manzouri. 2004. "Analysis of unreinforced masonry structures using elastic/viscoplastic models." In *Proc., Sísmica 2004-6°Congresso Nacional de Sismologia e Engenharia Sísmica Livro de Actas*, 137–150. Guimaraes, Portugal: Universidade do Minho.

Simo, J. C., and T. J. Hughes. 2006. *Computational inelasticity.* New York: Springer.

Simo, J. C., and R. Taylor. 1986. "A return mapping algorithm for plane stress elastoplasticity." *Inte. J. Numer. Methods Eng.* 22 (3): 649–670. https://doi.org/10.1002/nme.1620220310.

Spada, A., G. Giambanco, and P. Rizzo. 2009. "Damage and plasticity at the interfaces in composite materials and structures." *Comput. Methods Appl. Mech. Eng.* 198 (49–52): 3884–3901. https://doi.org/10.1016/j.cma.2009.08.024.

Tang, H., F. Barthelat, and H. Espinosa. 2007. "An elasto-viscoplastic interface model for investigating the constitutive behavior of nacre." *J. Mech. Phys. Solids* 55 (7): 1410–1438. https://doi.org/10.1016/j.jmps.2006.12.009.

Tarque, N. 2011. "Numerical modelling of the seismic behaviour of adobe buildings." Ph.D. dissertation, Dept. of Civil Engineering and Architecture, Univ. of Pavia.

Van der Pluijm, R., H. Rutten, and M. Ceelen. 2000. "Shear behaviour of bed joints." In Vol. 3 of *Proc., 12th Int. Brick/Block Masonry Conf., IB2MaC*, 1849–1862. Madrid, Spain: Construction and Architectonic Technology, Dept. of the Polytechnic, Univ. of Madrid.

Vermeltfoort, A. T., and T. Raijmakers. 1993a. *Deformation controlled tests in masonry shear walls: Part 1*. Rep. No. B-92-1156. Eindhoven, Netherlands: Eindhoven Univ. of Technology.

Vermeltfoort, A. T., and T. Raijmakers. 1993b. *Deformation controlled tests in masonry shear walls: Part 2*. Rep. No. TUE/BKO/93.08. Eindhoven, Netherlands: Eindhoven Univ. of Technology.